Journal of Materials Chemistry A

COMMUNICATION

View Article Online
View Journal

Cite this: DOI: 10.1039/c6ta09306j

Received 27th October 2016
Accepted 3rd January 2017

DOI: 10.1039/c6ta09306j

www.rsc.org/MaterialsA

Spontaneous linker-free binding of polyoxometalates on nitrogen-doped carbon nanotubes for efficient water oxidation†

Gil Yong Lee,‡[abc] Insu Kim,‡[b] Joonwon Lim,[abc] Moon Young Yang,[c] Dong Sung Choi,[abc] Yujin Gu,[b] Youngtak Oh,[abc] Seok Hun Kang,[abc] Yoon Sung Nam*[bc] and Sang Ouk Kim*[abc]

Efficient water oxidation remains a principal challenge for clean fuels *via* water splitting. Polyoxometalates (POMs) are promising water oxidation catalysts in a neutral medium but their application is commonly limited by low electrical conductivity and poor adhesiveness arising from bulky and electrically insulating ligands. Here we report linker-free spontaneous binding of tetracobalt-based polyoxometalates (Co_4POMs) on nitrogen-doped carbon nanotubes (NCNTs) *via* electrostatic hybridization. Protonated nitrogen-dopant sites at NCNTs enable linker-free immobilization of the Co_4POMs and fluent electron transfer in the resultant Co_4POM/NCNT hybrid structures, as demonstrated by the low overpotential of 370 mV for the water oxidation at pH 7. Accordingly, the hybrids exhibit fast reaction kinetics with a turnover frequency of 0.211 s^{-1} at 2.01 V *vs.* RHE. Density functional theory calculation proposes that POMs vertically align at the NCNT surface exposing the maximal catalytic surfaces. This work suggests a reliable route to highly efficient water oxidation catalysis by employing POMs under neutral conditions and NCNTs as self-binding nanoelectrodes in a synergistic well-oriented hybrid structure.

Introduction

Water splitting is a promising approach for clean and sustainable energy supply.[1,2] The rate-determining reaction step in water splitting is the water oxidation reaction, which requires an inherently high endothermic reaction barrier,[3,4] proton-coupled electron transfer (PCET),[5,6] and multiple-electron transfer.[7–9] Enormous research efforts have been devoted to the efficient catalysts for water oxidation. Typically, earth-scarce metal oxide catalysts, including ruthenium and iridium oxides, have been reported to exhibit high water oxidation efficiencies under acidic and basic conditions.[10,11] Unfortunately, their rarity and high price restrict a large scale application. Earth-abundant oxide catalysts of first-row transition metals have shown efficient electro-catalytic activity for water oxidation with moderate overpotential and high reaction currents in basic media.[12,13] By contrast, only a few catalysts, including cobalt-based oxygen evolving catalysts and polyoxometalates (POMs), are known to show high activity for water oxidation while maintaining their original structure under neutral conditions.[14–16]

POMs are stable three-dimensional metal-oxo clusters, comprising d-electron transition metals coordinated with oxyanions.[17,18] The transition metal atoms are usually in high oxidation states, making them attractive catalysts for the oxidation of various organic compounds.[19,20] Recently, POMs have been reported to efficiently catalyze the water oxidation under neutral conditions owing to their notable redox properties,[21,22] strong persistence against oxidative and hydrolytic degradation,[15,17] and excellent compatibility with aqueous environments.[19] Nonetheless, their closed polyionic structure encapsulated by bulky anionic ligands generates strong electrostatic repulsion among POMs, which makes it difficult to prepare a structurally stable catalytic layer on an electrode.[23–25] Additionally, the low electrical conductivity of POMs (about 10^{-3} to 10^{-1} S cm^{-1}) requires the use of well-designed nanostructured electrodes with high conductivity and large surface area for efficient electro-catalysis.[26] To this end, adhesive polymers or molecular linkers have been commonly employed to attach the POMs at the conductive electrode nanostructures.[27,28] The adhesive interlayers result in undesirable electrical resistance, which may impose limitations on the overall catalytic performance of POMs. Even though it has been reported that oxidized nanocarbons can immobilize POMs by spontaneous reduction, the electrically resistive oxygen functional groups still remain.[29–33]

In this work, we present the linker-free spontaneous binding hybrid system of tetracobalt-based polyoxometalates (Co_4POMs,

[a]National Creative Research Initiative Center for Multi-Dimensional Directed Nanoscale Assembly, Daejeon 34141, Republic of Korea

[b]Department of Materials Science and Engineering, Daejeon 34141, Republic of Korea

[c]KAIST Institutes for the NanoCentury, KAIST, Daejeon 34141, Republic of Korea. E-mail: yoonsung@kaist.ac.kr; sangouk.kim@kaist.ac.kr

† Electronic supplementary information (ESI) available: Experimental section, Fig. S1 to S14 and Tables S1 to S4. See DOI: 10.1039/c6ta09306j

‡ These authors contributed equally to this work.

$[Co_4(H_2O)_2(PW_9O_{34})_2]^{10-}$) on nitrogen-doped carbon nanotubes (NCNTs) for efficient electrolysis of water at a neutral pH. Among various POMs with different metal centers, Co_4POMs are known to have high catalytic activity for water oxidation under neutral conditions, earth-abundant metal center,[18] high resistance against oxidative degradation, and economic feasibility.[20] The readily protonated N-dopant sites of NCNTs offer chemically favorable direct binding sites for spontaneous immobilization of the Co_4POMs *via* electrostatic interactions.[34,35] In addition, N-dopants increase electrical conductivity by increasing the charge carrier density in the conjugated system of graphitic carbons. First-principles calculations revealed that the balanced intermolecular interactions among Co_4POMs, the N-dopant site, and the delocalized π-electron system of sp^2-hybridized carbons in the NCNTs yield vertically oriented Co_4POMs at the NCNT surface. This oriented structure without organic linkers is highly beneficial for water oxidation catalysis by the maximal exposure of metal catalytic sites of POMs to the surrounding electrolytes and facile electron transfer at the bare interface between Co_4POMs and NCNTs. Taking advantage of this optimal structure, Co_4POM/NCNT hybrids exhibited outstanding catalytic activity for water oxidation under neutral conditions, showing a Tafel slope of 203 mV decade^{-1} and a turnover frequency (TOF) of 0.211 s^{-1}.

Results and discussion

Co_4POMs used in this work were synthesized as described elsewhere,[15] and their spectroscopic and electrochemical properties were confirmed using UV-Vis absorption spectroscopy, Fourier transform infrared (FT-IR) spectroscopy, and cyclic voltammetry (CV) (Fig. S1 and S2, ESI†).[15,36] NCNTs were prepared by thermochemical treatment of commercially available multi-walled carbon nanotubes (MWCNTs) under ammonia environments, which effectively induces N-doping at the graphitic wall of CNTs.[37] For the spontaneous binding of Co_4POMs at the NCNT surface, an aqueous solution of Co_4POM (25 mmol L^{-1}) was simply mixed with the NCNT dispersion in an aqueous solution of pH 5 (0.3 mg mL^{-1}). In an appropriate pH range, the negatively charged Co_4POMs are spontaneously associated with the positively charged protonated N-dopants at the NCNT wall (Fig. 1a). To determine the exact pH range for spontaneous binding, the surface charge states of Co_4POMs and NCNTs were determined using zeta potential measurements in the pH range of 3–9 (Fig. 1b). Typically, Co_4POMs are chemically stable and negatively charged over the wide pH range due to the anionic nature of the POM ligands,[36,38] while NCNTs are positively charged below pH 5 by the active protonation of N-dopants with lone pair electrons. The oppositely charged states of Co_4POMs and NCNTs trigger a straightforward strong anchoring of Co_4POMs at electro-conductive NCNT surfaces.

Transmission electron microscopy (TEM) analysis revealed that Co_4POMs were self-assembled at individual particle level at the NCNT surface (Fig. 1c–e). The average particle size of Co_4POMs on the NCNT wall was about 1 nm, the typical size of an individual Co_4POM particle.[39,40] Scanning transmission electron microscopy (STEM) images reveal that the electron-rich

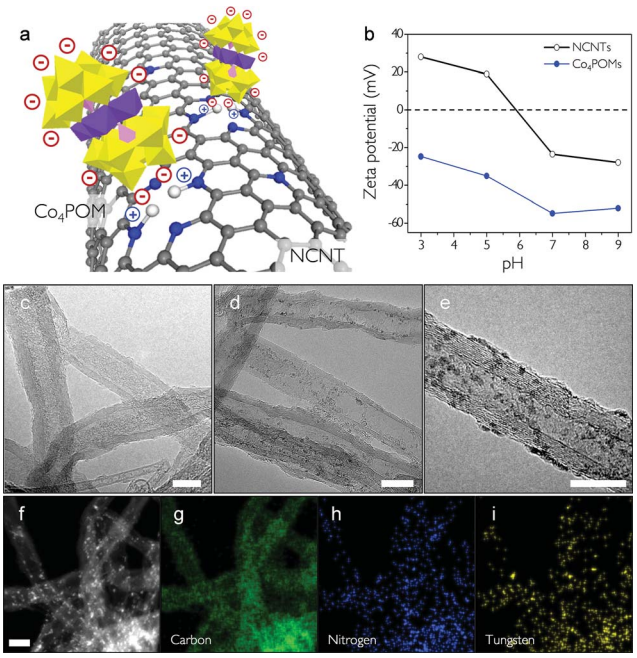

Fig. 1 (a) Schematic representation of spontaneous Co_4POMs binding at N-dopants of the NCNT surface *via* electrostatic interactions. Gray, blue, and white balls represent carbon, nitrogen, and hydrogen atoms, respectively. (b) Zeta potentials of NCNTs (black) and Co_4POMs (blue) as a function of pH. The TEM image of (c) bare NCNTs and (d and e) Co_4POM/NCNT hybrids. (f) Z-contrast high-angle annular dark-field (HAADF) TEM image. EDS elemental mapping of (g) $K\alpha_1$ emission of carbon, (h) $K\alpha_1$ emission of nitrogen, and (i) $L\alpha_1$ emission of tungsten of the Co_4POM/NCNT hybrids; scale bar represents 10 nm.

Co_4POMs were uniformly and individually distributed over the entire surface of NCNTs (Fig. 1f). Energy-dispersive X-ray spectroscopy (EDS) elemental mapping illustrates that tungsten and cobalt elements of Co_4POMs overlap with the carbon and nitrogen elements of NCNTs (Fig. 1g–i and S3, ESI†). As a control experiment, Co_4POMs were mixed with pristine undoped CNTs under the same experimental conditions used for Co_4POM/NCNT hybrid formation. Co_4POMs were barely deposited on the pristine CNT surfaces (Fig. S4, ESI†). Obviously, the N-dopant sites are primarily responsible for the spontaneous immobilization of Co_4POMs at NCNT surfaces.

Chemical structures of the Co_4POM/NCNT hybrids were characterized by Raman and FT-IR spectroscopies. The Raman spectrum of the Co_4POM/NCNT hybrids was compared with those of Co_4POMs and bare NCNTs (Fig. 2a). The spectra of NCNTs and hybrids exhibit distinct D and G bands of defective disordered and crystalline graphitic sites at the NCNT surface, respectively. The intensity ratio of the D and G bands (I_D/I_G) of the Co_4POM/NCNT hybrids and bare NCNTs are 0.87 and 1.18, respectively. The lower I_D/I_G ratio of the Co_4POM/NCNT hybrids signifies that Co_4POMs were principally grafted at N-dopant sites.[41,42] The characteristic FT-IR peaks for Co_4POMs were detected at 1037 cm^{-1} (P–O stretching), 943.9 cm^{-1} (W–O stretching), and 884.2 cm^{-1} and 731.8 cm^{-1} (W–O–W bending) (Fig. S1 and S5, ESI†).[36,43] The unique spectrum of Co_4POMs clearly appeared in the Co_4POM/NCNT hybrids, confirming that the chemical nature of Co_4POMs was not damaged during the hybridization process.

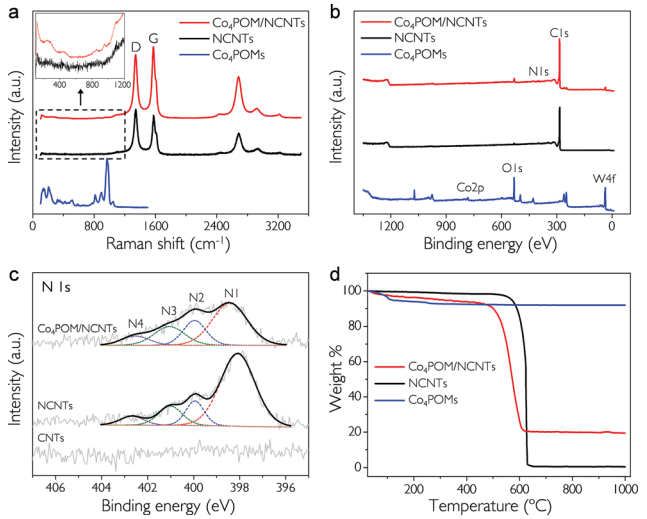

Fig. 2 (a) Raman spectra of Co_4POMs (blue), NCNTs (black), and the Co_4POM/NCNT hybrids (red). The inset indicates the expanded Raman spectra of NCNTs and Co_4POM/NCNT hybrids in the range of 100–1200 cm^{-1}. (b) XPS survey spectra of Co_4POMs (blue), NCNTs (black), and the Co_4POM/NCNT hybrids (red). (c) N 1s XPS spectra of CNTs, NCNTs, and the Co_4POM/NCNT hybrids. N1, N2, N3, and N4 correspond to pyridinic, pyrrolic, quaternary, and oxidized nitrogen. (d) TGA diagrams of Co_4POMs (blue), NCNTs (black), and the Co_4POM/NCNT hybrids (red) in O_2 (10 °C min^{-1}).

Elemental compositions and bonding configuration of the Co_4POMs, NCNTs and Co_4POM/NCNT hybrids were further investigated using X-ray photoelectron spectroscopy (XPS) (Fig. 2b and c). The distinctive features of Co_4POM/NCNT hybrids, compared with NCNTs, appeared in the W 4f and Co 2p peaks, which verify the successful immobilization of Co_4POMs at NCNT walls (Fig. S6, ESI†). The configurational variations of N-dopants were examined to characterize the bonding sites (Fig. 2c). The deconvoluted N 1s spectrum of NCNTs, with N doping content of 1.60 at%, exhibited distinctive peaks for pyridinic nitrogen (N1) at 398 eV, pyrrolic nitrogen (N2) at 399.7 eV, quaternary nitrogen (N3) at 401 eV, and oxidized nitrogen (N4) at 402.6 eV, respectively (Table S1, ESI†).[44–46] Interestingly, the peak intensity of pyridinic nitrogen, which principally undergoes protonation under acidic conditions, substantially decreased after the electrostatic hybridization. This verifies that the pyridinic nitrogen plays the role of major binding sites for Co_4POMs.

Mass content of the Co_4POM/NCNT hybrids was determined by thermogravimetric analysis (TGA) (Fig. 2d). Co_4POMs exhibited a minor weight loss of 7.9 wt% mainly due to the evaporation of bound water molecules, while NCNTs showed a major loss of 99.3 wt% (carbon burnout). Co_4POM/NCNT hybrids exhibited a weight loss of 80.0 wt%, indicating that the mass content of the Co_4POM in the hybrid structure was about 21.0 wt%, which agrees well with the inductively coupled plasma mass spectrometry (ICP-MS) analyses for cobalt (Fig. S7, ESI†). Notably, decomposition of the Co_4POM/NCNT hybrids occurs at an appreciably lower temperature compared to bare NCNTs. The transition metals (cobalt and tungsten) in Co_4POM may serve as catalysts for the oxidation of neighboring graphitic carbons.[47,48]

To better understand the spontaneous linker-free binding of Co_4POMs at the NCNT surface, density functional theory (DFT) calculations were carried out and determined the interfacial binding energies between Co_4POMs and NCNTs depending on the surface conditions of NCNTs and the conformational states of Co_4POMs. Chemical structures and calculation parameters used in the DFT calculations were in good agreement with the experimental data (Fig. S8 and Table S2, ESI†). The bare CNT surface can be approximated using a graphitic monolayer (Fig. 3a, b and S9a, b, ESI†). To evaluate the effects from N-dopants, a graphitic N atom and four pyridinic N atoms sharing two atomic vacancies were designed at the surface of the graphitic layer (Fig. S9c and d, ESI†). Pyridinic N dopants with 1 and 2 protonated sites were designed and denoted as pyridinic 4N–1H^+ and pyridinic 4N–2H^+, respectively (Fig. S9e and f, ESI†).

Co_4POM is found to be repulsive against both the pristine undoped graphene layer and N-doped graphene layer without protonation, due to the delocalized π-electrons over the layer, although the repulsion weakened with N-doping as a result of the charge polarization between the N atom and the neighboring C atoms (Fig. 3c, S10 and Table S3, ESI†).[49–51] Notably, significant attractive interactions were observed after the protonation of N-dopant sites. Pyridinic 4N–2H^+ exhibited a binding energy of −68.1 kcal mol^{-1}, which is comparable to the previously reported porphyrin-based catalysts (−80.1 kcal mol^{-1}) and covalently connected catalysts (about −88 kcal mol^{-1}).[52,53] This result supports that Co_4POMs can bind to the protonated N-dopants of the NCNT surface in a stable manner solely *via* electrostatic interactions. This is fully consistent with

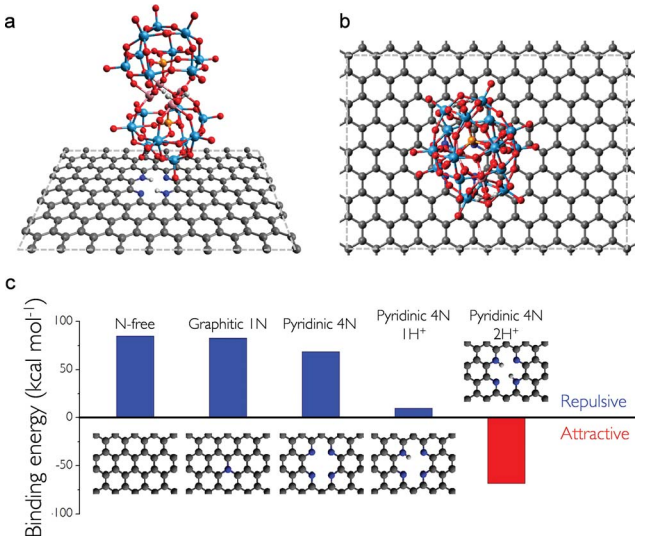

Fig. 3 Computational analysis for Co_4POM/NCNT hybrids. (a) Side and (b) top views of Co_4POM on the pyridinic 4N–2H^+ graphene layer. Red, cyan, orange, pink, white, and gray balls represent oxygen, tungsten, phosphorous, cobalt, hydrogen, and carbon atoms, respectively. Dashed lines indicate the periodic unit cell used in this work. (c) Calculated binding energies for different binding species.

our experimental finding for the formation of Co_4POM/NCNT hybrids. Significantly, Co_4POMs turn out to be energetically more favorable when they bind perpendicular to the NCNT surface (−68.1 kcal mol^{-1}), whereas the parallel binding mode significantly weakens the attractive interaction (−25.5 kcal mol^{-1}) (Fig. S11, ESI†). For the undoped pristine graphene layer, both perpendicular and parallel binding of the Co_4POM exhibited a repulsive force. These results indicate that the protonated N-dopant site is critically important for the spontaneous perpendicular binding of POM catalysts.

The anchoring stability of Co_4POM at the NCNT surface in our hybrids was experimentally confirmed by the residual amounts of Co_4POMs as a function of incubation time in a 0.1 M sodium phosphate buffer solution (pH 7) at room temperature (Fig. S12, ESI†). In the beginning of incubation, about 15% of Co_4POMs were detached from the hybrids, presumably arising from the weakly bound interfaces (*i.e.*, Co_4POM could bind to pyridinic 4N–1H$^+$ sites, or bind in parallel at the NCNT surface). Afterwards, the Co_4POM/NCNT hybrid structure remained stable without noticeable changes in the loading quantity of POMs.

Water oxidation behaviors of the Co_4POM/NCNT hybrids deposited on glassy carbon electrodes were analyzed in 0.1 M sodium phosphate at pH 7. A typical three-electrode configuration was used, with an Ag/AgCl reference electrode and a platinum wire counter electrode. Compared with bare NCNTs and Co_4POMs, Co_4POM/NCNT hybrids exhibited much higher current and significantly lower onset potential for the catalytic current, 1.6 V *vs.* RHE (Fig. 4a). This value corresponds to the overpotential of 370 mV. Bare NCNTs and Co_4POMs exhibited some faradaic current with the overpotential of 530 mV and 690 mV, respectively. As a reference sample with organic binding linkers, polyethyleneimine (PEI)-functionalized CNTs, denoted 'PEI/CNTs', were prepared and decorated with Co_4POMs under the same experimental conditions as the Co_4POM/NCNT hybrid formation. Protonated PEI/CNTs have been used as positively charged conducting substrates, which can realize electrostatic hybridization into Co_4POM/PEI/CNTs. Overpotential of the Co_4POM/PEI/CNT hybrids, 400 mV, was higher and their oxidation current was appreciably lower than those of Co_4POM/NCNT hybrids. For the quantitative comparison of their reaction kinetics, linear regions in the linear sweep voltammetry curves were fitted to Tafel plots (Fig. 4b). The resultant Tafel slopes of bare NCNTs, Co_4POMs, Co_4POM/PEI/CNT hybrids, and Co_4POM/NCNT hybrids were 340, 254, 387, and 203 mV decade^{-1}, respectively. The lowest Tafel slope demonstrates that the Co_4POM/NCNT hybrids exhibit the fastest reaction kinetics for water oxidation among all tested samples. It is noteworthy that the Tafel slope of Co_4POM/NCNT hybrids was appreciably lower than that of the previously reported Ru-based POM/polymer linker/CNT complex (296 mV per decade).[27] The excellent catalytic activity of Co_4POM/NCNT hybrids can be principally ascribed to the facile electron transfer with minimal the energy barrier at the Co_4POM/NCNT interface. In addition, the proposed perpendicular orientation of Co_4POMs at NCNT surfaces, as described above, may allow for the facile access of reactants to the catalytic active metal center (cobalt oxide) in

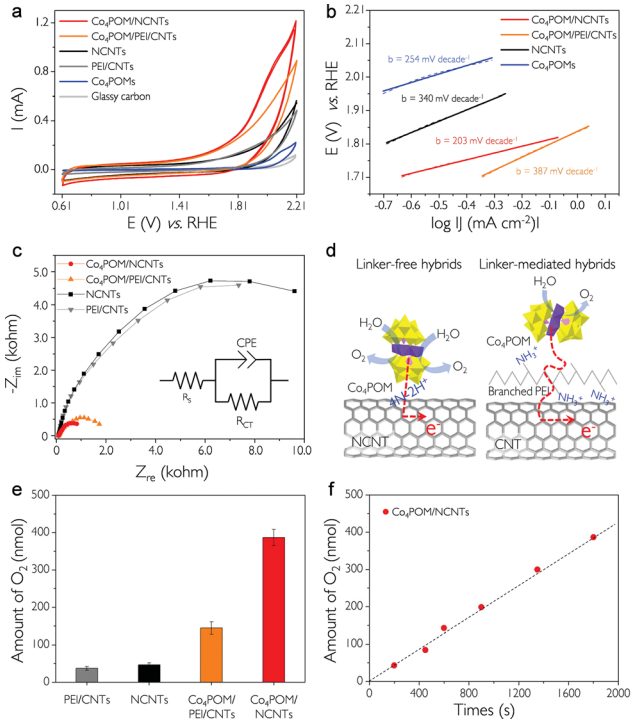

Fig. 4 (a) CV curves of a bare glassy carbon electrode (light gray) and Co_4POMs (blue), PEI/CNTs (gray), NCNTs (black), Co_4POM/PEI/CNT hybrids (orange), and Co_4POM/NCNT hybrids (red) deposited on the glassy carbon electrode. (b) Tafel plots of the Co_4POMs (blue), NCNTs (black), Co_4POM/PEI/CNT hybrids (orange), and Co_4POM/NCNT hybrids (red). (c) EIS of the PEI/CNTs (gray), NCNTs (black), Co_4POM/PEI/CNT hybrids (orange), and Co_4POM/NCNT hybrids (red) at 1.71 V from 20 kHz to 10 mHz. The inset indicates the equivalent circuit model. (d) Schematic of electron transfer from Co_4POMs to the NCNTs (linker-free hybrids) and PEI/CNTs (linker-mediated hybrids), respectively. (e) The amount of evolved oxygen of the PEI/CNTs, NCNTs, Co_4POM/PEI/CNT hybrids and Co_4POM/NCNT hybrids under 2.01 V for 30 min. (f) Time-dependent oxygen production of the Co_4POM/NCNT hybrids under 2.01 V. All potentials reported *versus* reversible hydrogen electrode (RHE).

Co_4POMs. We note that the Co_4POM/PEI/CNT hybrids exhibited more sluggish reaction kinetics than pristine Co_4POMs deposited on a glassy carbon electrode. The insulating organic linker caused undesirable contact resistance and decreased the overall catalytic efficiency.

To elucidate the structural validity of our linker-free hybrids regarding the efficient catalytic activity, charge transfer resistance (R_{CT}) is measured by an electrochemical impedance spectroscopy (EIS) analysis (Fig. 4c). The resulting Nyquist plots feature the semi-circles that correspond to the charge transfer process for water oxidation. The Co_4POM/NCNT hybrids exhibited a smaller diameter semi-circle than Co_4POM/PEI/CNT hybrids, indicating that the PEI inter-layer hinders charge transfer. With an equivalent circuit model (Fig. 4c, inset), the EIS data in the charge transfer reaction region were fitted for the quantitative comparison of catalytic activities (Fig. S13 and Table S4, ESI†). The linker-mediated Co_4POM/PEI/CNT hybrids exhibited R_{CT} around 2 times higher than the linker-free Co_4POM/NCNT hybrids confirming a significantly higher

charge transfer resistance caused by the PEI layer described in Fig. 4d. This systematic analysis on R_{CT} well-supports the outstanding electrochemical performance of the Co_4POM/NCNT hybrids.

The catalytic activity for water oxidation was quantitatively determined from oxygen evolution, which was analyzed using gas chromatography (GC) equipped with a gas-tight electrochemical cell (Fig. 4e). During operating at 2.01 V for 30 min (overpotential: 780 mV), Co_4POM/PEI/CNT hybrids produced 145 $\pm$ 16 nmol of oxygen, while linker-free Co_4POM/NCNT hybrids produced 387 $\pm$ 21 nmol of oxygen (approximately 2.7 times higher). The calculated turnover frequency (TOF) for Co_4POM/PEI/CNT hybrids and Co_4POM/NCNT hybrids at pH 7 were 0.079 s^{-1} and 0.211 s^{-1}, respectively. Notably, this TOF value of Co_4POM/NCNT hybrids is about 3.8 times higher than that of the polymer linker-based Ru_4POM/CNT complexes (0.055 s^{-1}).[27] These results indicate that the linker-free direct binding of Co_4POM/NCNT hybrids results in excellent electrocatalytic activity for water oxidation, compared with the typical hybrids of POMs and carbon supports (*i.e.*, MWCNT and graphene) with binding linkers.[27,28] Under the same experimental conditions, the bare PEI/CNTs and NCNTs produced only 37 $\pm$ 5 nmol and 47 $\pm$ 5 nmol of oxygen, respectively.

The amounts of charges generated from NCNTs and the Co_4POM/NCNT hybrids were plotted as a function of overpotential (Fig. S16, ESI†). Both of the electrodes generated capacitive current, derived from an electrical double layer below the potential of water oxidation. Their capacitive currents were similar, as shown in the overlapped dotted lines. Once the applied voltage exceeded the onset potential for water oxidation, Tafel slopes increased due to the faradaic currents generated by water oxidation, as shown in the solid lines. The observed overpotential values of NCNTs and Co_4POM/NCNT hybrids were about 580 mV and 380 mV, respectively. These values were consistent with the CV analysis results (Fig. 4a).

The water oxidation reaction rate can be calculated from the Tafel slope above the overpotential. The calculated reaction rate of Co_4POM/NCNT hybrids was 1.478 C V^{-1} above 380 mV, while that of NCNTs was 0.373 C V^{-1} above 580 mV. The reaction rate of Co_4POM/NCNT hybrids was about 4 times faster even under a much lower applied potential. The oxygen evolution of Co_4POM/NCNT hybrids was plotted as a function of time (Fig. 4f). During the electrolysis at 2.01 V, the amount of oxygen in the headspace linearly increased, ensuring no noticeable decomposition or degradation of the hybrids, as confirmed by EDS elemental mapping and XPS analysis of Co_4POM/NCNT hybrids before and after the water oxidation reaction (Fig. S14 and S15, ESI†). The calculated faradaic efficiency was higher than 90%.

These excellent catalytic activities of Co_4POM/NCNT hybrids could be attributed to the two principal advantages of the hybrid structures. The first is the facile drain of reaction charges during water oxidation through the linker-free interface between Co_4POMs and NCNTs. EIS analysis was performed for the measurement of the charge transfer resistance of the Co_4POM/NCNT hybrids, associated with the efficiency of the overall catalytic system (Fig. 4c). The linker-free immobilization increased the water oxidation activity of Co_4POMs by facilitating the electron transfer through the Co_4POM/NCNT interface, while NCNTs provide a reliable nanostructured pathway for the transfer of the generated electrons. The second significant advantage is related to the perpendicular orientation of Co_4POMs on the NCNT surface, as suggested by DFT theory calculation. It was proposed that the protonated Np sites (pyridinic 4N–2H^+) electrostatically attract the anionic oxo-cluster of the Co_4POMs and result in a perpendicular configuration of Co_4POMs at the NCNT surface based on binding energy calculation, as shown in Fig. 3 (Fig. S11, ESI†). Such a geometry allows the catalytic active sites (cobalt oxide) of Co_4POMs to be easily exposed to the surrounding electrolytes. Overall, this structural feature with a low charge barrier interface and desired molecular conformation results in the superior catalytic activity for water oxidation.

Conclusions

In summary, we have demonstrated linker-free Co_4POM/NCNT hybrids that yield excellent electro-catalytic activities for water oxidation under neutral conditions. Compared with the previous works employing cationic polymer linkers, this straightforward linker-free binding of Co_4POMs at the surface of NCNTs is critically beneficial for high efficiency water oxidation catalysis (Table S5, ESI†). It is noteworthy that polymer linkers could be degraded under oxidizing conditions, leading to a short catalytic active time (<400 s). While previous research studies on highly active Ru_4POM/graphene hybrids required additional (oxidizing) reagents ($Ru(bpy)_3^{2+}$ or Ce(IV)) or supporting electrolyte (1 M $Ca(NO_3)_2$), our Co_4POM/NCNT hybrid catalyst demonstrated highly active catalytic behavior with an overpotential of 370 mV, low Tafel slope of 203 mV $decade^{-1}$, and high turnover frequency (TOF) of 0.211 s^{-1} at pH 7 while maintaining a durable reaction time (<1800 s) without any additive. The measured catalytic activity is comparable to the results from Ru based POM/CNT hybrid catalysts exploiting the expensive earth rare Ru elements. This work demonstrates that the substitutional dopant sites at the graphene surface not only offer direct reliable binding sites for molecular hybrid structures but also induce specific molecular conformation at the interface for synergistic material performances.

Acknowledgements

We thank Prof. Hee-Tak Kim for his valuable comment on EIS analysis. This work was supported by the National Creative Research Initiative (CRI) Center for Multi-Dimensional Directed Nanoscale Assembly (2015R1A3A2033061) and Nano Material Technology Development Program through the National Research Foundation of Korea (NRF) funded by the Ministry of Science, ICT and Future Planning (2016M3A7B4905613). I. K., M. Y. Y., Y. G., and Y. S. N. were supported by the Korea CCS R&D Center (KCRC) grant (NRF-2014M1A8A1049303) funded by the Ministry of Science, ICT & Future Planning.

References

1 A. Bergmann, I. Zaharieva, H. Dau and P. Strasser, *Energy Environ. Sci.*, 2013, **6**, 2745–2755.
2 M. Gao, W. Sheng, Z. Zhuang, Q. Fang, S. Gu, J. Jiang and Y. Yan, *J. Am. Chem. Soc.*, 2014, **136**, 7077–7084.
3 Y. Surendranath, D. A. Lutterman, Y. Liu and D. G. Nocera, *J. Am. Chem. Soc.*, 2012, **134**, 6326–6336.
4 Y. Jiao, Y. Zheng, M. Jaroniec and S. Z. Qiao, *Chem. Soc. Rev.*, 2015, **44**, 2060–2086.
5 T. J. Meyer, M. H. Huynh and H. H. Thorp, *Angew. Chem., Int. Ed.*, 2007, **46**, 5284–5304.
6 C. J. Gagliardi, A. K. Vannucci, J. J. Concepcion, Z. F. Chen and T. J. Meyer, *Energy Environ. Sci.*, 2012, **5**, 7704–7717.
7 T. Takashima, K. Hashimoto and R. Nakamura, *J. Am. Chem. Soc.*, 2012, **134**, 18153–18156.
8 L. Trotochaud, J. K. Ranney, K. N. Williams and S. W. Boettcher, *J. Am. Chem. Soc.*, 2012, **134**, 17253–17261.
9 R. D. Smith, M. S. Prevot, R. D. Fagan, Z. Zhang, P. A. Sedach, M. K. Siu, S. Trudel and C. P. Berlinguette, *Science*, 2013, **340**, 60–63.
10 M. E. Lyons and S. Floquet, *Phys. Chem. Chem. Phys.*, 2011, **13**, 5314–5335.
11 Y. Lee, J. Suntivich, K. J. May, E. E. Perry and Y. Shao-Horn, *J. Phys. Chem. Lett.*, 2012, **3**, 399–404.
12 F. Cheng, J. Shen, B. Peng, Y. Pan, Z. Tao and J. Chen, *Nat. Chem.*, 2011, **3**, 79–84.
13 J. Suntivich, K. J. May, H. A. Gasteiger, J. B. Goodenough and Y. Shao-Horn, *Science*, 2011, **334**, 1383–1385.
14 M. W. Kanan and D. G. Nocera, *Science*, 2008, **321**, 1072–1075.
15 Q. Yin, J. M. Tan, C. Besson, Y. V. Geletii, D. G. Musaev, A. E. Kuznetsov, Z. Luo, K. I. Hardcastle and C. L. Hill, *Science*, 2010, **328**, 342–345.
16 J. B. Gerken, J. G. McAlpin, J. Y. Chen, M. L. Rigsby, W. H. Casey, R. D. Britt and S. S. Stahl, *J. Am. Chem. Soc.*, 2011, **133**, 14431–14442.
17 C. L. Hill, *Chem. Rev.*, 1998, **98**, 1–2.
18 H. Lv, Y. V. Geletii, C. Zhao, J. W. Vickers, G. Zhu, Z. Luo, J. Song, T. Lian, D. G. Musaev and C. L. Hill, *Chem. Soc. Rev.*, 2012, **41**, 7572–7589.
19 A. R. Howells, A. Sankarraj and C. Shannon, *J. Am. Chem. Soc.*, 2004, **126**, 12258–12259.
20 A. Sartorel, M. Bonchio, S. Campagna and F. Scandola, *Chem. Soc. Rev.*, 2013, **42**, 2262–2280.
21 A. Sartorel, M. Carraro, F. M. Toma, M. Prato and M. Bonchio, *Energy Environ. Sci.*, 2012, **5**, 5592–5603.
22 S. S. Wang and G. Y. Yang, *Chem. Rev.*, 2015, **115**, 4893–4962.
23 M. Sadakane and E. Steckhan, *Chem. Rev.*, 1998, **98**, 219–237.
24 A. Sartorel, M. Carraro, G. Scorrano, R. D. Zorzi, S. Geremia, N. D. McDaniel, S. Bernhard and M. Bonchio, *J. Am. Chem. Soc.*, 2008, **130**, 5006–5007.
25 Y. F. Song and R. Tsunashima, *Chem. Soc. Rev.*, 2012, **41**, 7384–7402.
26 E. Coronado and C. J. Gomez-Garcia, *Chem. Rev.*, 1998, **98**, 273–296.
27 F. M. Toma, A. Sartorel, M. Iurlo, M. Carraro, P. Parisse, C. Maccato, S. Rapino, B. R. Gonzalez, H. Amenitsch, T. Da Ros, L. Casalis, A. Goldoni, M. Marcaccio, G. Scorrano, G. Scoles, F. Paolucci, M. Prato and M. Bonchio, *Nat. Chem.*, 2010, **2**, 826–831.
28 M. Quintana, A. M. Lopez, S. Rapino, F. M. Toma, M. Iurlo, M. Carraro, A. Sartorel, C. Maccato, X. Ke, C. Bittencourt, T. Da Ros, G. Van Tendeloo, M. Marcaccio, F. Paolucci, M. Prato and M. Bonchio, *ACS Nano*, 2013, **7**, 811–817.
29 H. Li, S. Pang, X. Feng, K. Müllen and C. Bubeck, *Chem. Commun.*, 2010, **46**, 6243–6245.
30 R. Liu, S. Li, X. Yu, G. Zhang, Y. Ma and J. Yao, *J. Mater. Chem.*, 2011, **21**, 14917–14924.
31 R. Liu, S. Li, X. Yu, G. Zhang, S. Zhang, J. Yao and L. Zhi, *J. Mater. Chem.*, 2012, **22**, 3319–3322.
32 S. Wang, H. Li, S. Li, F. Liu, D. Wu, X. Feng and L. Wu, *Chem.–Eur. J.*, 2013, **19**, 10895–10902.
33 R. Liu, G. Zhang, H. Cao, S. Zhang, Y. Xie, A. Haider, U. Kortz, B. Chen, N. S. Dalal, Y. Zhao, L. Zhi, C. Wu, L. Yan, Z. Su and B. Keita, *Energy Environ. Sci.*, 2016, **9**, 1012–1023.
34 U. N. Maiti, W. J. Lee, J. M. Lee, Y. Oh, J. Y. Kim, J. E. Kim, J. Shim, T. H. Han and S. O. Kim, *Adv. Mater.*, 2014, **26**, 40–66.
35 J. M. Lee, J. Lim, N. Lee, H. I. Park, K. E. Lee, T. Jeon, S. A. Nam, J. Kim, J. Shin and S. O. Kim, *Adv. Mater.*, 2015, **27**, 1519–1525.
36 C. A. Ohlin, S. J. Harley, J. G. McAlpin, R. K. Hocking, B. Q. Mercado, R. L. Johnson, E. M. Villa, M. K. Fidler, M. M. Olmstead, L. Spiccia, R. D. Britt and W. H. Casey, *Chem.–Eur. J.*, 2011, **17**, 4408–4417.
37 J. M. Lee, J. S. Park, S. H. Lee, H. Kim, S. Yoo and S. O. Kim, *Adv. Mater.*, 2011, **23**, 629–633.
38 D. Lieb, A. Zahl, E. F. Wilson, C. Streb, L. C. Nye, K. Meyer and I. Ivanovic-Burmazovic, *Inorg. Chem.*, 2011, **50**, 9053–9058.
39 J. Sloan, Z. Liu, K. Suenaga, N. R. Wilson, P. A. Pandey, L. M. Perkins, J. P. Rourke and I. J. Shannon, *Nano Lett.*, 2010, **10**, 4600–4606.
40 T. Yamamoto, Y. Umemura and Y. Einaga, *Dalton Trans.*, 2013, **42**, 16014–16020.
41 B. R. Sathe, B. A. Kakade, A. Kushwaha, M. Aslam and V. K. Pillai, *Chem. Commun.*, 2010, **46**, 5671–5673.
42 Y. A. Li, N. H. Tai, S. K. Chen and T. Y. Tsai, *ACS Nano*, 2011, **5**, 6500–6506.
43 C. I. Cabello, M. G. Egusquiza, I. L. Botto and G. Minelli, *Mater. Chem. Phys.*, 2004, **87**, 264–274.
44 X. Li, H. Wang, J. T. Robinson, H. Sanchez, G. Diankov and H. Dai, *J. Am. Chem. Soc.*, 2009, **131**, 15939–15944.
45 D. H. Lee, W. J. Lee, W. J. Lee, S. O. Kim and Y. H. Kim, *Phys. Rev. Lett.*, 2011, **106**, 175502.
46 A. U. Haq, J. Lim, J. M. Yun, W. J. Lee, T. H. Han and S. O. Kim, *Small*, 2013, **9**, 3829–3833.
47 J. Q. Huang, Q. Zhang, M. Q. Zhao and F. Wei, *Carbon*, 2010, **48**, 1441–1450.
48 M. Wang, T. Li, Y. Yao, H. Lu, Q. Li, M. Chen and Q. Li, *J. Am. Chem. Soc.*, 2014, **136**, 18156–18162.

49 T. Schiros, D. Nordlund, L. Palova, D. Prezzi, L. Zhao, K. S. Kim, U. Wurstbauer, C. Gutierrez, D. Delongchamp, C. Jaye, D. Fischer, H. Ogasawara, L. G. Pettersson, D. R. Reichman, P. Kim, M. S. Hybertsen and A. N. Pasupathy, *Nano Lett.*, 2012, **12**, 4025–4031.
50 B. Wang, L. Tsetseris and S. T. Pantelides, *J. Mater. Chem. A*, 2013, **1**, 14927–14934.
51 W. J. Lee, U. N. Maiti, J. M. Lee, J. Lim, T. H. Han and S. O. Kim, *Chem. Commun.*, 2014, **50**, 6818–6830.
52 W. Orellana, *Chem. Phys. Lett.*, 2012, **541**, 81–84.
53 G. Mette, D. Sutter, Y. Gurdal, S. Schnidrig, B. Probst, M. Iannuzzi, J. Hutter, R. Alberto and J. Osterwalder, *Nanoscale*, 2016, **8**, 7958–7968.